
Article:
Brisset, Alexandra Helene Marie Brigitte orcid.org/0000-0003-3217-1106, Guichard, Florestan, Cessou, Armelle et al. (1 more author) (2021) Energy relaxation and heating in the afterglow of high electric field ns-discharges in ambient air using spontaneous Raman scattering. Plasma sources science & technology. 035013. ISSN 0963-0252

https://doi.org/10.1088/1361-6595/abe6e5

Energy relaxation and heating in the afterglow of high electric field ns-discharges in ambient air using spontaneous Raman scattering

Energy relaxation and heating in the afterglow of high electric field ns-discharges in ambient air using spontaneous Raman scattering

Alexandra Brisset[1], Florestan Guichard[2], Armelle Cessou[2] and Pierre Tardiveau[1]

[1] Université Paris-Saclay, CNRS, LPGP, 91405 Orsay, France
[2] Normandie Univ, UNIROUEN, INSA Rouen, CNRS, CORIA, 76000 Rouen, France

E-mail: alexandra.brisset@u-psud.fr

Abstract

The spatio-temporal rovibrational excitation and relaxation mechanisms of $N_2(X)$ in the post-discarge of a 10 ns high-voltage diffuse discharge are studied by Spontaneous Raman Scattering. It is shown that the vibrational excitation of nitrogen molecules remains high despite the strong electric fields applied during the discharge itself and the relaxation processes are similar to lower voltage ns discharges. The main differences with the lower field discharges are rather visible at the beginning of the discharge with a specific spatial volume distribution and a significant vibrational non-equilibrium between v=0,1 and v>1. The spatial distribution of the rovibrational excitation of the diffuse discharge is very wide radially, consistent with the sustainability of fields greater than 100 Td over nearly 8 mm during propagation. The initial rovibrational excitation is inhomogeneous along the axis. The gas temperature reaches up to about 1200 K close to the pin (85 kV, ambient air) while it remains below 500 K in the rest of the volume. It is possible to control the heating of the discharge without greatly modifying the energy transfer mechanisms by adjusting the duration of the voltage pulse. In terms of reactivity, high atomic oxygen densities seem to be very localized in the vicinity of the pin (10^{24} m^{-3} at 1.5 mm from the pin, corresponding to about 20 % dissociation). This inhomogeneity reflects the distribution of energy in the volume of the discharge. The main effects of humidity are also studied. It amplifies the fast heating and accelerates the decay of atomic oxygen in the post-discharge. No significant acceleration of the V-T relaxation of nitrogen due to the addition of water vapour was observed for the studied conditions. A shock wave was identified which is triggered at around 500 ns.

Keywords: spontaneous Raman scattering, nanosecond discharge, vibrational distribution, shock wave

1. Introduction

Stable and volume extended high power discharges can be generated in atmospheric air by applying to a sharp electrode very strong overvoltage, higher than several hundreds percents [1–4]. If the overvoltage is maintained throughout a time period which is short enough, less than a few tens of nanoseconds, the induced plasma keeps out of thermal equilibrium and the heating of the gas remains limited. Recent experimental studies on this kind of discharges also show that, despite natural shielding effect induced by the plasma, high electric fields can be sustained over larger areas than it is for common low voltage streamer discharges where high fields remain very localized [5,6]. Those field conditions are conducive to the generation of high energy electrons and subsequently to the efficient production of specific reactive species. Indeed, not only the density but also the nature of these species depend highly on the electron energy distribution function (EEDF) and therefore on the electric field [7–10].

Under high but very transient fields of streamer discharges, reactions induced in dry air by electronic impact produce mainly excited nitrogen, among which are $N_2(X^1\Sigma_g^+, v>1)$ vibrationally excited ground states, $N_2(A\ ^{3+}\Sigma_u)$ metastables and $N_2(B\ ^3\Pi_g)$, $N_2(C\ ^3\Pi_u)$ radiative states. These last three species contribute to the main channel of production of O atoms that leads to species oxidation [7] and fast heating [11]. Through this process, a high density of atomic oxygen is usually measured, due to the relatively low dissociation energy of oxygen (5 eV, while the typical mean energy of electrons is 1-3 eV). After the streamer front propagation, O atoms density is about 10^{16}-10^{17} cm^{-3}, corresponding to dissociation rates up to 40% [12]. On the other hand, the dissociation energy of nitrogen is much higher, about 10 eV, requiring higher fields to reach significant dissociation rates. For reduced fields around 150-200 Td, nitrogen dissociation is mostly initiated by $N_2(b^1\Pi_u, c^1\Pi_u, o^1\Pi_u, e^1\Pi, b^1\Sigma_u^+, c^1\Sigma_u^+, e^1\Sigma_u^+)$ and other excited states of high excitation energy (>12 eV) [11]. The produced $N(^2D)$ atoms react quickly with molecular oxygen to form nitric oxide and atomic oxygen ($O(^1D)$ or $O(^3P)$). For fields above 400 Td, ionisation of molecular nitrogen and oxygen drains an increasing fraction of the electron energy while vibrational excitation becomes negligible. Major positive ions are N_2^+ and N_4^+, N_2^+ ions being rapidly converted into N_4^+ by a three body reaction with nitrogen.

With small addition of hydrocarbons, volatil organic compounds (VOCs) or water vapor, a large range of new species, in particular H, OH radicals and H_2O_2 can also be produced. The OH radical is known to be one of the most reactive species in air plasmas. Its spatio-temporal distribution is often determined to understand plasma kinetics. In a photo-triggered atmospheric discharge of N_2/C_3H_8 and $N_2/O_2/C_3H_8$ [13], hydroxyl radicals were proved to play a more efficient oxidation role than atomic oxygen. In the high-fields nanosecond corona discharge studied in this work, it was shown that the efficiency of production of OH was about 1-2 molecules per 100 eV [14] against 0.2 molecules per 100 eV in the photo-triggered discharge run in relatively comparable conditions. However, at very high overvoltage (>65 kV), the efficiency of production of OH seems to diminish with specific energy defined as the ratio of the energy dissipated in the discharge with its volume [14]. Therefore, a complete study of species densities must be done to estimate the energy efficiency associated to a working condition of high field discharges. Also, compared to pure air conditions, excited states of nitrogen play additional roles in these complex admixtures. In particular, they can dissociate the hydrocarbon and water molecules, the latter requiring 5.1 eV. In the conditions of [13], it was demonstrated that the hydrocarbon is primarily dissociated by quenching of nitrogen metastable states, producing propene and hydrogen. The dissociation of water molecules is also mostly induced by collisions with nitrogen metastables $N_2(A)$, atomic oxygen $O(^1D)$ or dissociative recombination with H_3O^+ [15].

Because high field non-equilibrium diffuse discharges might produce high amounts of reactive species in a large volume of gas, without consuming too much energy, they have great interest for many applications such as gas effluent treatment [13], assisted combustion [16], flow control [17] or decontamination. In such applications, the way the electrical energy is transferred into the gas through chemical and hydrodynamical processes is also a point to be detailed. For instance, non-thermal plasma sources have shown to help the ignition of flamable mixtures [18–20] or to stabilize flames [21,22], highlighting the key role of plasma induced radicals chemistry compared to usual heating processes. In this context, non thermal plasma discharges help the ignition of lean mixtures, reduce ignition delays and have interesting features such as the possibility to create several kernels of ignition in particular gas mixtures [23]. Also, flow control performances for flow separation or fluid mixing, can be much enhanced by plasma actuators. At high speed, flow control is done by injection of species accelerating vibration to translation (V-T) energy transfers [17]. The use of plasma actuators has much developped recently but allows local control only. Recent studies take interest in the controlled storage and transport of the actuators with the flow and the release of the energy contained in their internal modes at the targeted location.

In air, for moderate fields (10 to 100 Td), $N_2(v)$ stores most of the energy and is the dominant actor of energy relaxation processes. It is also the major contributor to atomic nitrogen formation and other species such as NO. The energy storage and relaxation mecanisms in the afterglow of filamentary nanosecond discharges in air have already been identified and studied [24–27]. They depend on the different energy transfer processes between rotational, vibrational and electronic states. In time and space, the population distribution evolves according to these energy transfers and different numerical models are used to describe it. The general mechanisms in atmospheric air are the following. Just after the discharge, most of the energy is stored in the vibrational levels of nitrogen ground state [28–30] dominantly through inelastic electron impact collisions and cascade mechanisms from electronically exited states of nitrogen. The vibrational distribution is out of equilibrium and high vibrational levels are more populated as compared to the equilbrium distribution [24,30]. A more or less significant part of the energy is

also converted to fast heating, mostly through the dissociation of oxygen by quenching of electronically excited states of nitrogen [11]. Then, energy transfers between vibrational levels of nitrogen (V-V transfers) bring the vibrational distribution back to equilibrium in about 100 µs [29]. Finally, through diffusion and vibration to translation (V-T) transfers, the plasma relaxes to complete equilibrium in a few tens of ms.

This paper is the continuation of a series of papers that explore these processes in nanosecond air discharges [24,25]. The later papers described not only the gas temperature and the vibrational distribution functions of N_2 and O_2 but also presented the change in density of the major species and highlighted hydrodynamic effects (shock wave and fresh gas circulation in the vicinity of the pin. Here, the purpose is first to determine the possible impacts of the structural and physical modifications of the diffusion discharge generated under extreme electric fields, on these mechanisms and on the spatial distribution of the energy. For instance, one can wonder if the energy still dominantly spreads to vibrational levels of nitrogen. Indeed the fraction of deposited electron energy in vibrational excitation of nitrogen drops abruptly above 100 Td while much higher fields are maintained on the volume [5]. This paper also explores the influence of water vapor on the energy relaxation mechanisms. It was demonstrated that water vapor increases fast heating in high field regions of pulsed air corona discharges [9,29,31]. Several mechanisms are responsible for the increase of fast heating among which OH formation and fast V-V transfers of N_2-H_2O system followed by the fast V-T transfer of water molecules [29].

Relaxation mechanisms of nitrogen in air plasmas requires complex measurements. Spontaneous Raman Scattering (SRS) is used in this work to provide complete spatio-temporal information on the plasma post-discharge processes by measuring the rovibrational temperatures of dominant species. The rotational temperature of $N_2(X)$ is assimilated to the gas temperature which enables to estimate the rate of fast heating and can also be used for the determination of rate constants for kinetic models. Finally, through temperature and density measurements, pressure evolution can reveal pressure waves or fresh gas inlet in time.

2. Experimental setup

2.1 The discharge system

The discharge is created in a pin-to-plane configuration of electrodes being separated by a gap of 18 mm. A complete description of the device is presented in [32]. The pin is made of tungsten with a 100 µm curvature radius. The plane is a 5 cm diameter copper plate connected to the ground. An FID-type technology power supply provides positive high voltage nanosecond pulses, applied to the pin. Two shapes of voltage pulse are used having voltage rise times of 2 ns each and a full width at half maximum of 5 ns or 10 ns. These two pulses will be referred to as, respectively, channel 1 and channel 2. The maximum voltage amplitudes vary from 65 kV to 85 kV. The discharge is run at 5 Hz, in a controlled atmosphere reactor flowing synthetic air at 1 $L.min^{-1}$ in the direction of the pin-to-plane axis to which water vapour can be added from 25 to 73 % of relative humidity (RH). Relative humidity is controlled by flowing a portion of the air flow into an evaporator upstream of the reactor. To avoid condensation effects, the evaporator was placed in a temperature-controlled bath 5°C below the ambient temperature and the water saturated air flow was diluted with a minimum dry air flow just after the exit of the evaporator, limiting achievable relative humidity to 73%. Water is added upstream of the reactor passing through a controlled temperature water evaporator and a dilution system. RH is measured inside the reactor with a standard Testo 635 hygrometer.

The electric signals for a pulse of 85 kV in channel 1 are given in Figure 1. The energy is deposited through the electric field as long as the voltage is applied, up to 10ns. A small part of this energy is consumed in ionization and direct excitation processes during the propagation and establishment of the discharge, and most of the energy deposit occurs after the junction (1.6 ns). The energy is then distributed over several pathways such as rapid heating and vibrational excitation of N_2.

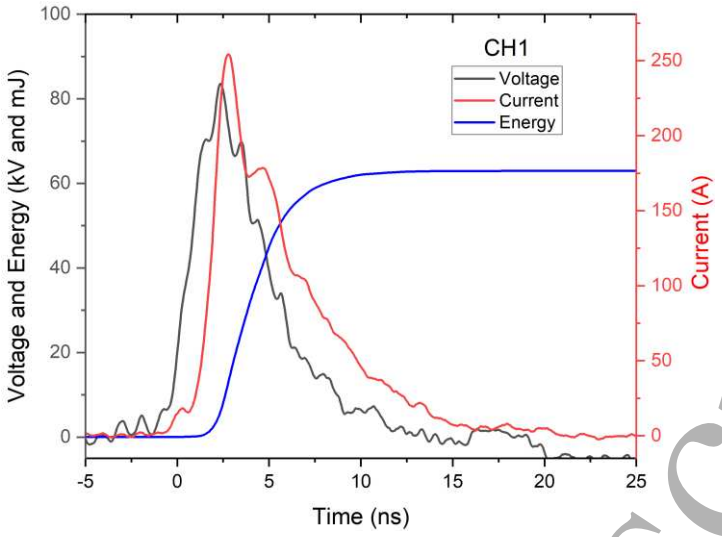

Figure 1: Voltage, current and energy of a 85 kV pulse in channel 1. The instant t=0 ns corresponds to the instant at which light is detected at the pin.

2.2 The detection device

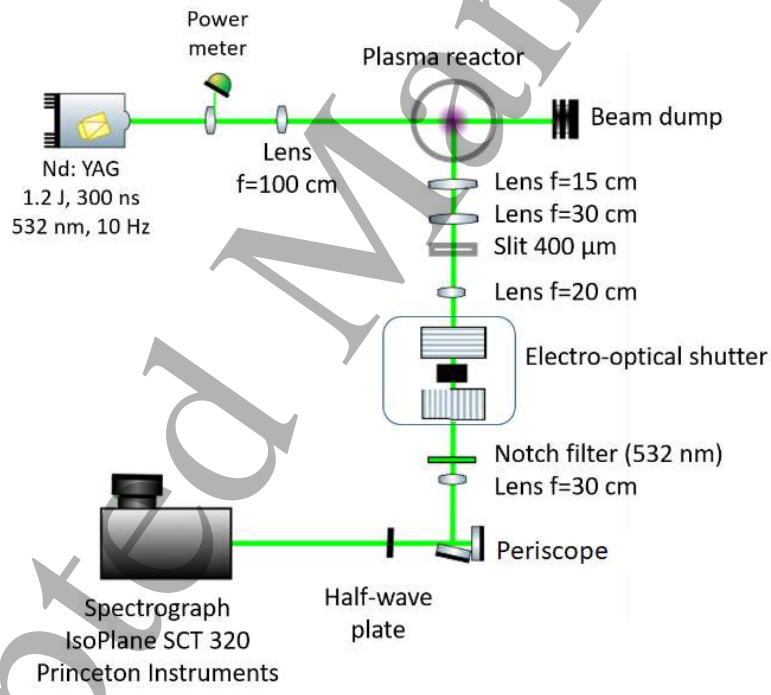

Figure 2: Experimental set-up of the detection system.

An overview of the detection setup is presented in Figure 2. The laser is an Agilite pulsed Nd:YAG by Continuum working at 1.2 J with a pulse duration of 300 ns at a frequency of 10 Hz. The light is collected perpendicularly to the laser beam allowing linewise measurements. To this end, a lens of 1000 mm focal length is used to focalise the laser over a region of 2.4 mm long and 170 µm width. The collected signal first goes through a 400 µm slit to remove part of the light emitted by the discharge from the volume surrounding the probed region. Then, a KD*P Pockels cell (LAP-50) by Quantum Tech. with two crossed polarizers is used as an electro-optical shutter to cut the light during the camera reading process [33]. A notch filter (NF03-532E (Semrock)) at 532 nm removes the Rayleigh emission. A periscope rotates the image before the Raman signal is finally dispersed by a spectrograph IsoPlane SCT 320 equipped with a 600 gr.mm^{-1} grating blazed at 500 nm and a back-illuminated

CCD camera (Pixis 400B). A CCD camera offers a better signal to noise ratio and the fast gating is guaranteed by the Pockels cell system. A binning is done over 300 µm. Therefore, each measurement provides information on 8 regions of interest along the laser beam. As the grating in the spectrometer is polarization dependent, the beam polarization is rotated after the scattering by a half-wave plate to optimise the transmission of the spectrograph.

All the measurements presented in this paper are averaged over 300 ns. In all the figures of section 4 and 5, the measurements taken below 10 µs are plotted at the instant corresponding to the middle of the acquisition gate (150 ns for the measurement starting at the beginning of the discharge, 350 ns for the measurement starting at 200 ns of the post discharge) and the time averaging is indicated as a horizontal error bar, on figure 4 only for clarity. From 10 µs, the effect of the 300 ns averaging is neglected.

The choice of the 600 gr.mm^{-1} grating enables to probe multiple species simultaneously due to its large spectral range (547 to 680 nm). Nevertheless, gas temperature measurements are possible with a precise determination of the slit function [34]. Figure 3 shows typical Raman spectra of ground-states of O_2 and N_2 in the first 300 ns of the post-discharge (black) and without discharge (red).

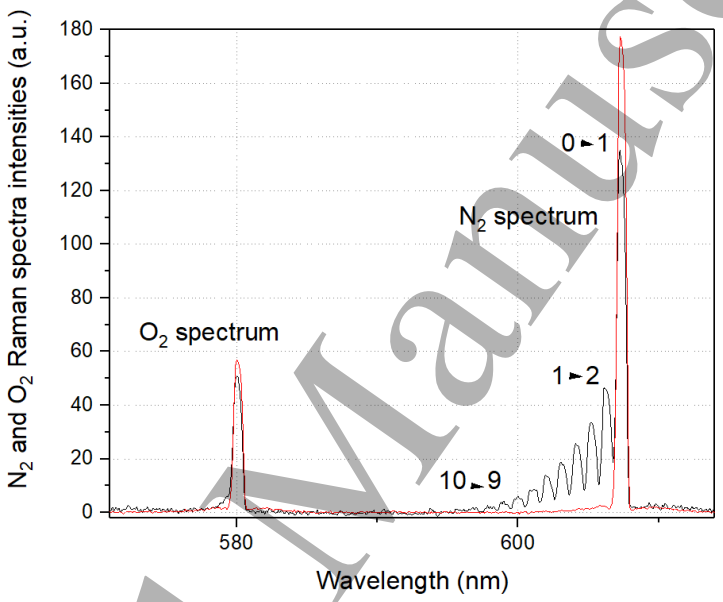

Figure 3: O_2 and N_2 Raman spectra with discharge (black) and without discharge (red) in the first 300 ns of the post-discharge at 85 kV, at 1.5 mm from the high voltage electrode. The spectrum is integrated over 400 discharges.

2.3 Time synchronization

Measurements cover the total duration of the post-discharge, from the first hundreds of nanoseconds to the late milliseconds. Since the discharge pulse generator has a jitter of 1.5 µs, it is necessary to use a complex synchronisation system in the first tens of microseconds of the post-discharges to get an accurate phasing of the measurements with the discharge. A master clock is set at 10 Hz. The laser is driven by this master clock with a delay of 155 µs ± 2 ns. The discharge generator is triggered from the master clock, only one pulse out of two, considering the delay of the voltage pulse (750 µs ± 1.5 µs) and the probed time of measurement in the post-discharge. The generator delivers a TTL signal precisely 256 ns (± 300 ps) before the voltage pulse which is used as an input in a logical gate. If the logical gate detects this signal and the pulse laser simultaneously, it triggers the electro-optical cell. Therefore, for times before 50 µs, the temporal uncertainty is given by the length of the laser pulse, 300 ns. For temporal measurement over 50 µs, the logical gate is removed and all measurements are kept in order to increase the acquisition rate and then the signal/noise ratio setting the temporal jitter to 1.5 µs.

3. Spectral analysis method

3.1 Spontaneous Raman scattering spectra

The experimental Raman scattering spectra of N_2 and O_2 are compared to theoretical Raman spectra given by the code described in [34]. Its general characteristics are reminded below. Figure 3 showed that in the first instants of the post-discharge high vibrational levels of the ground state of N_2 are populated, contrarily to O_2, and this distribution is not a Boltzmann one, including a strong overpopulation of the vibrational level v=0. This highly non-equilibrium behaviour of N_2 confirms that despite the very high fields and the new diffuse structure of the discharge, it still remains in the scope of the typical non-equilibrium discharges already observed and analysed [17,24,25,27]. Therefore, several population distribution functions have to be considered to correctly describe the discharge and to determine the degree of non-equilibrium between the different population levels.

3.2 Fitting model according to the state of the plasma

3.2.1 At thermodynamic equilibrium $T_{rot} = T_{vib} = T$

A model at thermodynamic equilibrium proves to be suitable for describing spatial positions at the limit and out of the discharge and at all positions after returning to equilibrium in the late stages of the post-discharge. The population of the ground state vibrational levels of one species can be described by the following equation:

$$N_{v,J} = N\frac{(2J+1)g_J exp\left(-\frac{hcE_{vib}(v)}{kT}-\frac{hcE_{rot}(v,J)}{kT}\right)}{Q_{vib}(T)Q_{rot}(v,T)} \quad (1)$$

where $N_{v,J}$ is the density of the vibrational level v and rotational level J, N the total density, g_J is the degeneracy of the rotational level J, E_{vib} is the vibrational energy of the vibrational level v and E_{rot} is the rotational level of the level (v,J), Q_{vib} and Q_{rot} are the vibrational and rotational partition functions, h is the Planck constant, c is the celerity of light (in cm.s^{-1}) and k is the Boltzmann constant. The dimension of energies is in cm^{-1}.

3.2.2 At high vibrational non-equilibrium $T_{rot} \neq T_{v_{01}} \neq T_{v_{1v}}$

A three temperatures model is necessary to describe the high vibrational non-equilibrium preceding vibration relaxation, where $T_{v_{01}}$ is the temperature determined from the population of levels 0 and 1 and $T_{v_{1v}}$ is determined from the population of all higher vibrational levels.

$$N_{v=0,J} = N\frac{(2J+1)g_J ex\,p\left(\frac{hc\left(E_{vib}(v=1)-E_{vib}(v=0)\right)}{kT_{v_{01}}}-\frac{hcE_{vib}(v=1)}{kT_{v_{1v}}}-\frac{hcE_{rot}(0,J)}{kT_{rot}}\right)}{Q_{vib}(T_{v_{01}},T_{v_{1v}})Q_{rot}(0,T_{rot})} \quad (2)$$

$$N_{v>0,J} = N\frac{(2J+1)g_J ex\,p\left(-\frac{hcE_{vib}(v)}{kT_{v_{1v}}}-\frac{hcE_{rot}(v,J)}{kT_{rot}}\right)}{Q_{vib}(T_{v_{01}},T_{v_{1v}})Q_{rot}(v,T_{rot})} \quad (3)$$

3.2.3 At vibrational equilibrium $T_{rot} \neq T_{vib}$

A two temperatures model, with a single temperature T_{vib} to describe all vibrational levels of the population distribution of N_2(X) and a different rotational temperature T_{rot}, is used to correctly describes the population distribution at times just following vibrational relaxation.

$$N_{v,J} = N\frac{(2J+1)g_J exp\left(-\frac{hcE_{vib}(v)}{kT_{vib}}-\frac{hcE_{rot}(v,J)}{kT_{rot}}\right)}{Q_{vib}(T_{vib})Q_{rot}(v,T_{rot})} \quad (4)$$

3.3 Species densities and pressure determination

The density $\mathbf{N^s}$ of a species *s*, as derived in detail in [24], is proportional to the intensity of the Raman signal $\boldsymbol{I^s}$ of that species (area of the population distribution). The instrumental function Λ(λ) being normalised such as $\int_0^\infty \mathbf{\Lambda(\lambda)d\lambda = 1}$, it is determined by the following relation:

$$I^s(T, T_{v_{01}}, T_{v_{1v}}) = C^{exp} \times N^s \times \sum_{v,J}\left(\sum_{OQS} f^s_{v,J}(T, T_{v_{01}}, T_{v_{1v}}) \times \left(\frac{\partial \sigma_R}{\partial \Omega}\right)^s_{v,J\rightarrow v',J'}\right) \quad (5)$$

where $\boldsymbol{f^s_{vJ}\left(T, T_{v_{01}}, T_{v_{1v}}\right)}$ is the temperature dependent distribution function and $\left(\frac{\partial \sigma_R}{\partial \Omega}\right)^s_{v,J\rightarrow v',J'}$ is the Raman scattering cross section taking into account the O,Q and S Raman branches and C^{exp} is an experimental constant determined by the product of the laser irradiance, the solid angle of detection, the length of the detection volume and the efficiency of the collection system.

The ratio of intensities of the Raman scattering signal with discharge and without discharge by keeping all other parameters identical enables to eliminate the experimental constant, leading to the following expression:

$$\frac{N^s_d}{N^s_{ref}} = \frac{I^s_d \times \sum_{v,J}\left(\sum_{OQS} f^s_{v,J}(T_{ref}) \times \left(\frac{\partial \sigma_R}{\partial \Omega}\right)^s_{v,J\rightarrow v',J'}\right)}{I^s_{ref} \times \sum_{v,J}\left(\sum_{OQS} f^s_{v,J}(T, T_{v_{01}}, T_{v_{1v}}) \times \left(\frac{\partial \sigma_R}{\partial \Omega}\right)^s_{v,J\rightarrow v',J'}\right)}$$

where the index *d* stands for the case with discharge and the index *ref* stands for the case without discharge at room temperature.

Atomic oxygen does not produce any Raman signal as it has no rotational or vibrational states. However, its density can be determined with the evolution of the ratio of O_2 and N_2 molecules compared with the equilibrium ratio. This method assumes that nitrogen dissociation is negligible and that atomic oxygen is the major stable specie produced in the discharge. Therefore, the dissociation rate of O_2 can be expressed as:

$$\tau_{dissociation}(O_2) = \frac{1/2\, n(\mathrm{O})}{n(\mathrm{O_2}) + 1/2\, n(\mathrm{O})}$$

Finally, the gas pressure *P* is derived from gas density and temperature measurements, by using the ideal gas law and still neglecting nitrogen dissociation.

4. Spatial and temporal evolution of rovibrational temperatures of $N_2(X)$ in the post-discharge

4.1. Typical vibrational and rotational temperature evolutions in dry air under very high voltages

To better characterize the vibrational and rotational temperature evolutions of the ground state of N_2 in the diffuse discharge, preliminary experiments were conducted in dry air. Indeed, several studies have already identified the vibrational population and relaxation mechanisms of various dry air discharges [27,30,34,35]. Results on the axis of the discharge, at 1.5 mm from the pin and 85 kV are presented in Figure 4. The temporal evolution of the different temperatures is typical of low temperature air atmospheric discharges. The vibrational population distribution is described by two vibrational temperatures during the first 10 µs (three temperature model): the temperature estimated from the populations of levels 0 and 1 is close to 1500 K and the temperature describing the higher levels is close to 5000 K. The vibrational equilibrium is reached within 10 to 50 µs. On time scales of 50 to 500 µs the gas temperature increases through energy transfers from vibrational to translational modes. Then, temperatures decrease by diffusion. The vibrational excitation of nitrogen molecules measured on the first 300 ns of the post-discharge are due to direct impact from low energy electrons of the discharge and de-excitation of high excited levels of nitrogen.

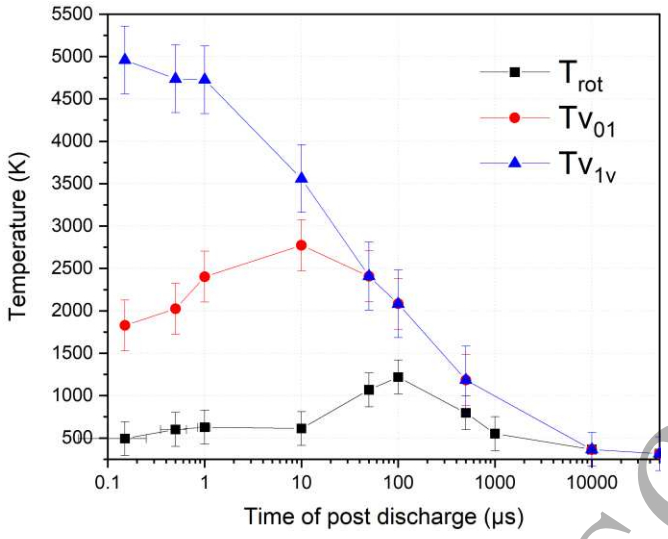

Figure 4: Temporal evolution of the rovibrational temperatures of $N_2(X,v)$ during the post-discharge for channel 1, at 85 kV, at 1.5 mm from the pin and in dry air. The horizontal uncertainty indicated for T_{rot} expresses the time averaging which applies to every measure presented in this paper.

The rotational temperature of N_2 is assimilated to the gas temperature. On the first 300 ns of the post-discharge, the gas temperature is about 500 K ± 200 K at 1.5 mm from the pin and 85 kV. Gas heating on such time scales is known as fast heating and has been accurately described by several authors at low and high fields [11,36,37]. In dry air, fast heating is dominated by the dissociative quenching reaction involving O_2 and electronically excited states of nitrogen, specifically $A^3\Sigma_u^+$, $B^3\Pi_g$, $C^3\Pi_u$, $a'^1\Sigma_u^-$ and $a^1\Pi_g$. Fast heating is also due to the quenching of $O(^1D)$ with N_2 and O_2 and at high fields (>400 Td), the dissociation of O_2 and N_2 by electronic impact and other reactions involving charged particles becomes important. Atomic nitrogen lines have been observed by optical emission spectroscopy in this discharge only in the first millimeter around the pin, supporting the very active character of the discharge, locally.

Excitation processes of heavy particles during the discharge are mostly governed by electrons and are extremely fast due to the high speed of electrons. On the contrary, heavy-heavy particle interactions take place over up to several milliseconds and progressively modify the population distributions. In atmospheric air, the fastest mechanism for vibrational relaxation involving heavy particles is vibration- vibration (V-V) energy transfer, restoring vibrational equilibrium over 10 to 50 µs. In the meantime, vibration-translation (V-T) transfers remain low. However, an increase of the gas temperature about 100 K is observed at the pin showing that there is an ongoing chemical heating [27] but moderate, probably balanced by the adiabatic cooling induced by the development of a shock wave (between 500 ns et 1 µs, see section 5).

V-T transfers dominate from 10 to 500 µs resulting in gas heating. At the pin where a large amount of energy was stored in the vibrational levels of nitrogen, gas heating is strong and at 100 µs gas temperature reaches a maximum of 1200 K. Once all the energy stored during the discharge into internal modes of the gas molecules has been released to heat, the gas cools down by thermal diffusion and convection.

4.2. Effect of humidity at high voltage

Most applications, from air depollution or flow control to plasma assisted combustion take place in ambient air. The study of the effect of humidity on the discharge behaviour recently had a renewed interest caused by its significant impact on heating mechanisms and post-discharge kinetics [9,29,30,38] and it is the purpose of the following section.

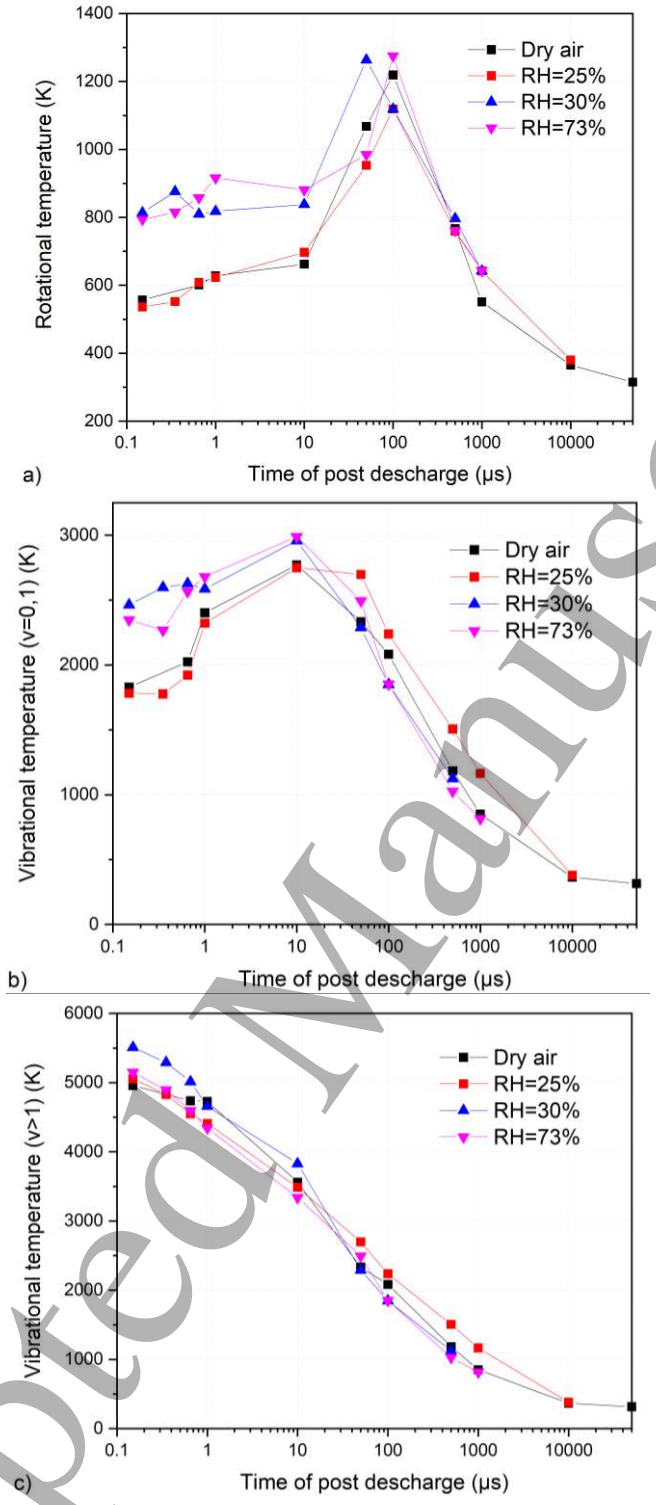

Figure 5: Temporal evolution of the rotational temperature of $N_2(X)$ a), the vibrational temperature of v=0,1 b) and the vibrational temperature of v>1 c) during the post-discharge at 85 kV (channel 1) for different relative humidity at 1.5 mm from the pin.

Rovibrational temperature measurements were performed at 85 kV for four different relative humidity levels: dry, 25 %, 30 % and 73 %. In ambient air, the relative humidity measured was 30 %, corresponding to a water concentration of 1.1 % at 28 °C. The water concentration variations were of the order of 0.1 % which is negligible for this study. Figure 5 shows the time evolution of rotational (a) and vibrational (b, c) temperatures of $N_2(X)$ at 1.5 mm from the pin for each RH level. The mechanisms which govern the population distribution of the high vibrational levels of N_2 during the post-discharge at 85 kV

are relatively similar in dry and humid air. However, during the first microseconds, the excitation of low vibrational levels and more conspicuously the rotational excitation are significantly stronger for water vapour concentrations over 1.1 %.

The rotational temperature in ambient air reaches 800 K ± 200 K in less than 300 ns which is about 300 K more than in dry air. The same threshold behaviour has been observed already on the discharge propagation itself and the reasons for it could be the effect of water aggregates at high humidity levels [39]. Indeed, it was observed in [39] that the relative humidity affects significantly the propagation speed, the spatial distribution of the intensity of the emitted light, the energy and the gas temperature of the discharge when the relative humidity is above 30% and the voltage rise rate is above 30 kV.ns^{-1} (those effects, are only observed at very high applied electric fields). In particular, the propagation speed of the discharge abruptly slows down by about 30% and the light intensity profiles show a twice stronger emission in the vicinity of the pin (<2 mm) but is slightly weaker in the rest of the gap. In terms of electric energy, the effect of water vapour seems to be relatively independent of the water vapor concentration (from 25 to 73 % of relative humidity), it induces a slight decrease of the energy from 62 to 54 mJ per pulse at 85 kV. Also, it appeared that already at the end of the discharge pulse (10 ns), the gas temperature is slightly increased in presence of water vapor at 85 kV. It was suggested in [39] that these aspects could be linked to a sudden change of the size distribution of water clusters above 30% relative humidity as observed in [40] and to unclear field dependent effects. In air, at atmospheric pressure, the size distribution of water clusters shifts from a bi-gaussian distribution of low mean size water clusters below RH=30%, to a single gaussian distribution with a higher mean size water cluster above RH=30%. Large water clusters can affect the electronic attachment and UV-photon absorption and therefore affect the discharge properties, such as the propagation speed. The effect on fast heating (720+60 K [39]) could partially be induced by ions (mainly water cluster ions). Their mobility in the very strong electric fields close to the pin could be high enough to transfer some of their energy significantly. In this work, Figure 5 shows that the same threshold effect of humidity on gas heating is accentuated and clear at later times in the early post discharge. Since Raman scattering measurements are averaged over 300 ns, the gas heating indicated in the first nanoseconds of the discharge and post-discharge are partly due to longer time range processes (up to 150 ns) than those mentioned above. Some explanations are suggested hereafter.

The increased fast heating due to single neutral water vapour molecules has been specifically described in a numerical study by Komuro and al. [9] for atmospheric air discharges. It was shown that additional fast heating comes from fast H_2O-H_2O V-T transfers as well as the exothermic formation of OH. The reactions involved in [9] take into account the vibrational kinetics of $N_2(v)$, $O_2(v)$ and $H_2O(v)$ as well as reactions involved in OH creation but not the contribution of the ions. They are summarised below.

OH can be formed by electronic impact from H_2O:

$$H_2O + e^- \rightarrow H + OH + e^- \quad (6)$$
$$H_2O + e^- \rightarrow OH^- + H \quad (7)$$
$$H_2O + e^- \rightarrow H^- + OH \quad (8)$$

where the energy threshold for reactions (6) to (8) are respectively 7, 3.58 and 4.36 eV.

Important processes of OH formation are also the branching reaction of H_2O and $O(^1D)$ and the dissociative quenching of $N_2(a)$ by H_2O:

$$O(^1D) + H_2O \rightarrow 2\ OH \quad (9)$$
$$N_2(a) + H_2O \rightarrow N_2(v) + OH + H \quad (10)$$

However, the molar fraction of H_2O is low and $O(^1D)$ atoms are efficiently quenched by N_2 and O_2 so a relatively small part of the electrons and $O(^1D)$ atoms interacts with H_2O. Finally, the major contribution to gas heating involving OH is the following two-steps process (where M Є $[O_2(v), N_2(v)]$):

$$H + O_2 + M \rightarrow HO_2 + M \quad (11)$$
$$O(^3P) + HO_2 \rightarrow OH + O_2(v) \quad (12)$$

Another major source of fast heating due to water vapour comes from the very fast V-T transfers of $H_2O(v)$, orders of magnitude faster than for nitrogen and oxygen. The V-T time rates of the stretching (v_1, v_3) and bending (v_2) modes of H_2O are

respectively 100 ns and 40 ns in atmospheric air at 300 K. In addition, in [21], resonant and near-resonant modes of respectively O_2(v=1) and N_2(v=1) with H_2O (0,1,0) have been identified also explaining the faster vibrational relaxation of O_2 in humid air:

$$O_2(v) + H_2O \rightarrow O_2(v\text{-}1) + H_2O\ (v_2) \quad (13)$$
$$N_2(v) + H_2O \rightarrow N_2(v\text{-}1) + H_2O(v) \quad (14)$$

where the time constant of reaction (13) is 3 µs and the time constants of equation (14) is 100 µs at 300 K and drops down to 15 µs at 1000 K. Since an important part of the energy is stored into N_2(v) and O_2(v), it is possible that (14) followed by fast V-T relaxation of H_2O(v) represents a significant role in fast heating in the high field diffuse discharge, which should decrease the population of the vibrational levels 1 and over.

Figure 5b shows that the population distribution of the first vibrational level is increased at high relative humidity (RH>30%) and below 1 µs. This experimental result is in contradiction with a simulation described in [41], describing the V-T energy transfer of a streamer in dry (0.1% H_2O) and humid air (2.0%H_2O). The simulation showed that the population distribution of the first vibrational level of nitrogen is nearly identical in dry and in humid air. However, this simulation describes a lower voltage streamer discharge and does not consider water clusters. At the moment, the reason why the experimental Tv_{01} is increased for RH>30% is not clear. Information describing the coupling of water molecules, clusters or ions ($H_x^+(H_2O)_n$) with individual vibrational modes of nitrogen may help to determine whether the presence of water clusters affects the vibrational distribution of N_2(X). Also, it cannot be excluded that, considering the uncertainty of the procedure for gas temperature below or close to 500K, Tv_{01} could be slightly affected and this increase could also be induced (or partly induced) by the uncertainty on T_{rot}. This would need further study.

4.3. Effect of voltage amplitude

In *[5]*, we observed clear changes in the field profile of the high voltage diffuse discharge as a function of the voltage amplitude. In particular, we observed a strong spatial extension of the field during propagation and also the sustaining of high fields, close to the critical ionization field in the plasma channel. In the presence also of high electron densities, the high-voltage electrical power densities are therefore particularly high. In order to know how far the rovibrational distribution of N_2(X) can be affected, measurements were made at 65 and 85 kV in ambient air (1.1 % water vapor). Figure 6 shows the time evolution of the rotational and vibrational temperatures of N_2(X) on the discharge axis at 1.5, 9 and 16.5 mm.

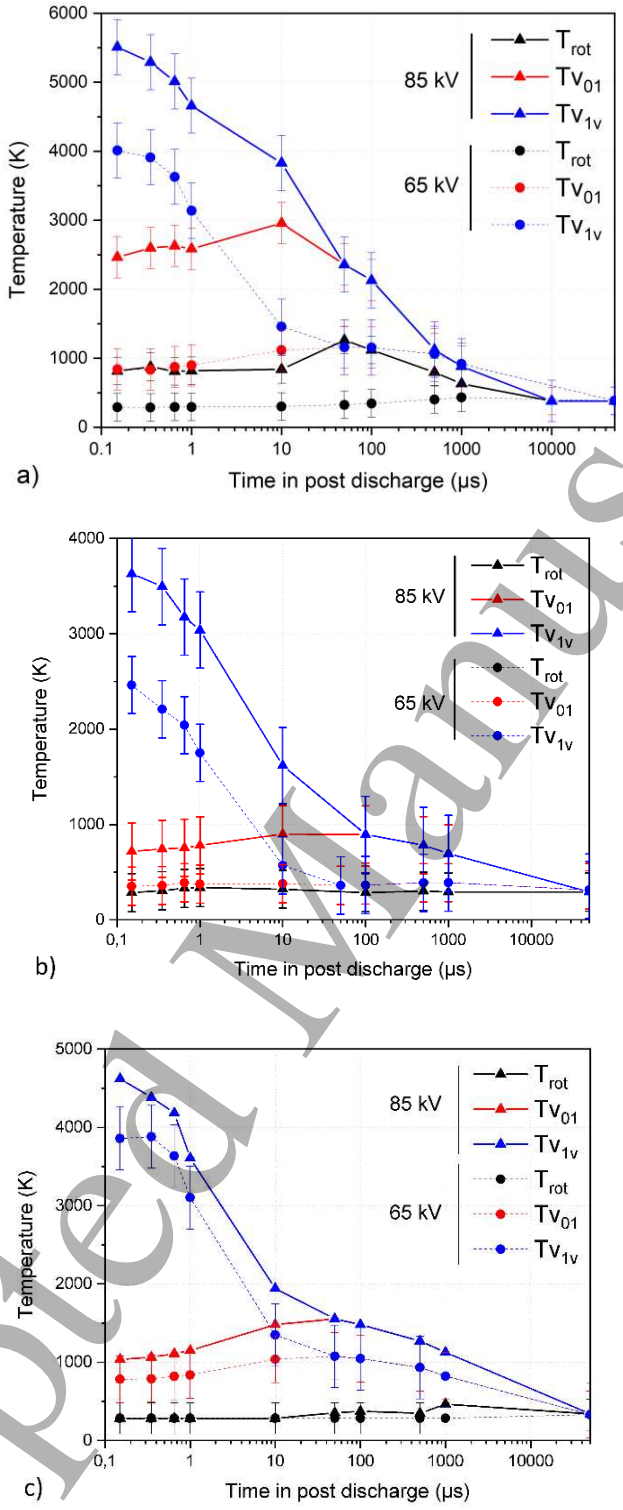

Figure 6: Temporal evolution of rovibrational temperatures of $N_2(X,v)$ during the post-discharge at 65 and 85 kV in ambient air (channel 1, RH=30 %) at 1.5 mm a) 9 mm b) and 16.5 mm c) from the pin.

At 1.5 mm and 65 kV, despite water vapour concentration higher than the threshold of 1%, there is no significant heating of the gas by fast heating mechanisms and the heating due to V-T transfers is also very limited ($T_{gas} \approx 450$ K at 500 µs). The vibrational distribution is still strongly out of equilibrium but the vibrational temperature is quite low: $Tv_{1v} = 4000$ K and

Tv_{01} = 1000 K. At 85 kV, the vibrational distribution of N_2 is excited at least up to level 10, while only the first 5 levels are observed at 65 kV, showing that the excitation mechanisms are favoured by the very high voltage. A probable explanation is that the electron density is higher at 85 kV or that the region around the pin where the field is high is extended. Another explanation could come from a different distribution of the energy of the electrons at 65 and 85 kV. In [5], it is said that the field distribution in the diffuse discharge favours the electronic excitation of N_2 over vibrational excitation and also ion formation. Thus, a large part of the vibrational excitation mechanisms of N_2 could be indirect mechanisms, requiring the prior formation of ions or excited states N_2^*. A possible explanation for the low vibrational excitation at 65 kV is therefore the lower proportion of vibrational excitation by quenching of excited states of molecular nitrogen.

At 9 mm and 65 kV, the vibrational excitation of N_2 is very limited and the temperature of the first vibrational levels (0,1) is at equilibrium with the gas temperature, considering the sensitivity limit of the method. The temperature of the vibrational levels higher than 1 still equalizes the other temperatures within 10 to 50 µs but there is practically no heating of the gas. At 85 kV, the vibrational excitation of the first levels is sufficient to be measured but the gas temperature remains below the detection limit.

At 16.5 mm, the differences between the vibrational excitation of the discharges at 65 and 85 kV are small. The vibrational temperatures are close and observe exactly the same temporal evolution. This could mean that the propagation phase has a very important role in the vibrational excitation of $N_2(X)$. At the plane level, the gas is only subjected to the conduction phase, contrary to the other positions where significant differences between the rovibrational distributions have been observed. In [5], the major differences in the distribution of the reduced fields between 65 and 85 kV have been observed during the propagation of the discharge, which can favour the excitation of the high excited states of nitrogen, whereas they were very close in the first instants following the junction at the plane.

In conclusion, it appears that at 65 kV, the vibrational relaxation mechanisms are similar and occur on the same time scales as at 85 kV, but the rovibrational excitation is weaker. The effect of the voltage is strongly dependent on the position along the pin-plane axis. At the pin, the heating of the gas is below the detection limit at 65 kV, suggesting a low production of excited states of N_2. At 9 mm, the temperature of the first vibrational levels (0,1) is at equilibrium with the gas temperature and at 16.5 mm the distributions of $N_2(X,v)$ are similar, suggesting that the propagation phase has an important role in the distribution of $N_2(X)$.

4.4. Effect of pulse shape

Increasing the pulse duration from 6 ns to 10 ns (switching from generator channel 1 to channel 2) does not fundamentally change the mechanisms governing the distribution of $N_2(X,v)$ and the relaxation of the energy (Figure 7). The succession of e-V, then V-V and V-T transfers still explains the evolution of the distributions and the characteristic times of these transfers are identical. However, a longer pulse duration while keeping all other parameters identical (the rise time is almost identical: 2.8 ns instead of 2 ns) favours a slight vibrational excitation during the discharge, especially in the weakly excited body of the discharge. At the pin, the heating of the gas is faster and more intense (up to 2000 K at 100 µs). The results obtained with the channel 2 in the diffuse discharge are close to those obtained with a pulse nearly twice as long but with lower voltages [34]. In [34], a FID generator is also used, operating at 10 Hz for a gap length of 6.5 mm. The amplitude of the pulse is 25 kV with a mid-point duration of 25 ns and a rise time of 5 ns. The evolution of the gas temperature is very similar to the case of the diffuse discharge. Just after the discharge, rapid heating leads to a temperature of 1000 K at 1.5 mm from the pin. For N_2, V-T processes between 10 and 100 µs lead to an increase of the translation temperature from 1000 K to 2000 K. The vibrational distribution, however, is different since it is almost at equilibrium at 1.5 mm from the pin, with 5800 K for the first vibrational levels and 7000 K for the other levels. The vibrational balance is nevertheless reached in 10-50 µs as well. After 100 µs, the stored vibrational energy has become low and temperatures decrease by diffusion and convection.

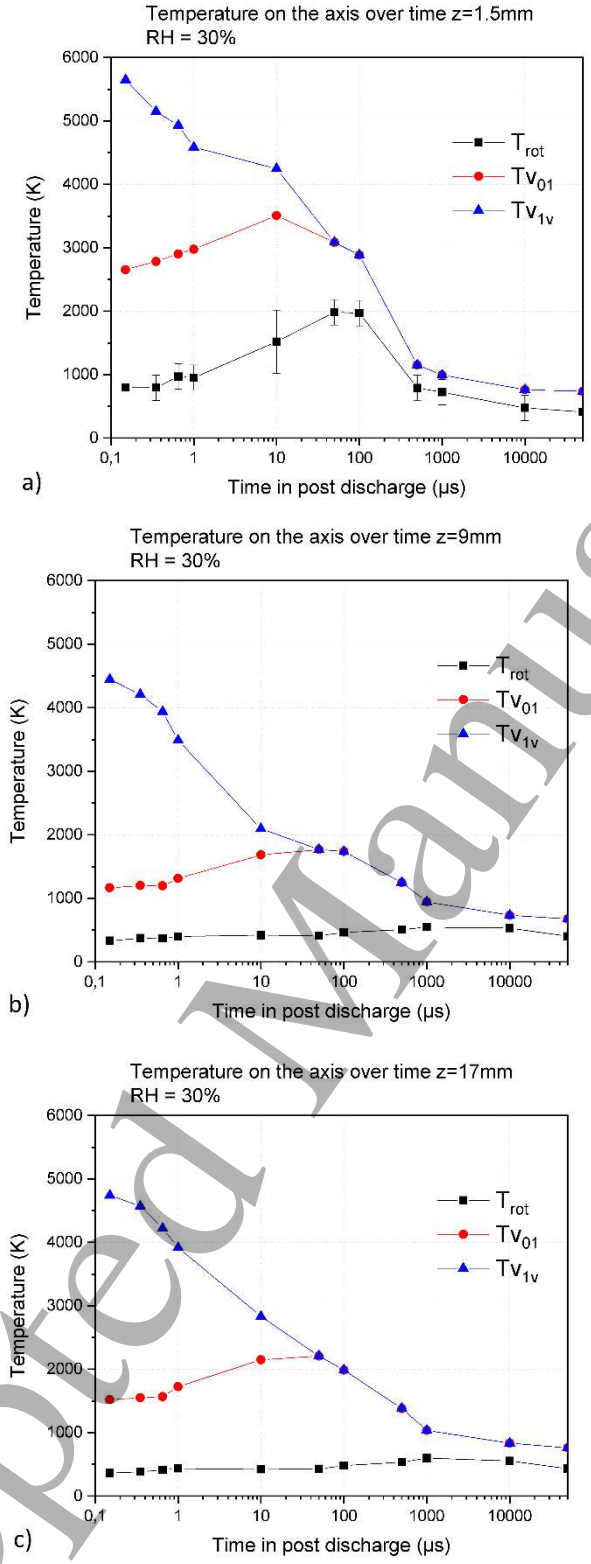

Figure 7: Temporal evolution of the rovibrational temperature of $N_2(X,v)$ during the post-discharge at 85 kV for channel 2 (rise time of 2.8 ns, full width high maximum of 10 ns) in ambient air at different positions along the axis a) 1.5 mm, b) 9 mm and c) 16.5 mm.

4.5. Radial distribution of the rovibrational temperatures of $N_2(X,v)$

Measures of the reduced electric field [5] showed that during the propagation of the discharge, fields higher than the critical ionisation field are maintained radially up to 8 mm off-axis, at mid-gap. The distribution of $N_2(X)$ is effectively spread radially over comparable radius. Figure 8 shows the radial distribution of $N_2(X,v)$ at 1.5 mm from the pin in the first 300 ns after the discharge (a) and at 500 µs (c) and at 9 mm from the pin at similar times (b) and (d), for a pulse of 85 kV (channel 1), in ambient air. The radial extension and shape of rovibrational temperatures depend on the considered temperature. In the vicinity of the pin, rotational and first vibrational levels temperature profiles are very picked whereas at mid-gap, they are large and homogeneous but with a sharp decrease at the edges. At longer times, the temperatures have spread and homogenised radially. Since the precise determination of temperatures at the edges of the plasma is relatively imprecise, especially in the centre of the gap (z=9 mm), where the excitation is limited, the radial expansion of the vibrational temperatures is not clearly visible in Figures 8 b and d. However, it is clearly visible at the pin, for Figures 8 a and c where the excitation radius has almost doubled (about 1 mm in the first 300 ns and about 2 mm at 500 µs). The rotational temperature is well defined only above 500 K, below it is affected by the instrumental function determination as can be clearly seen on Figure 8 b, c and d which have small oscillations of the rotational temperature due to slight differences of the instrumental function of each of the 7 regions of interest plotted. Indeed, the Raman rovibrational profiles are very similar between 300 and 500 K.

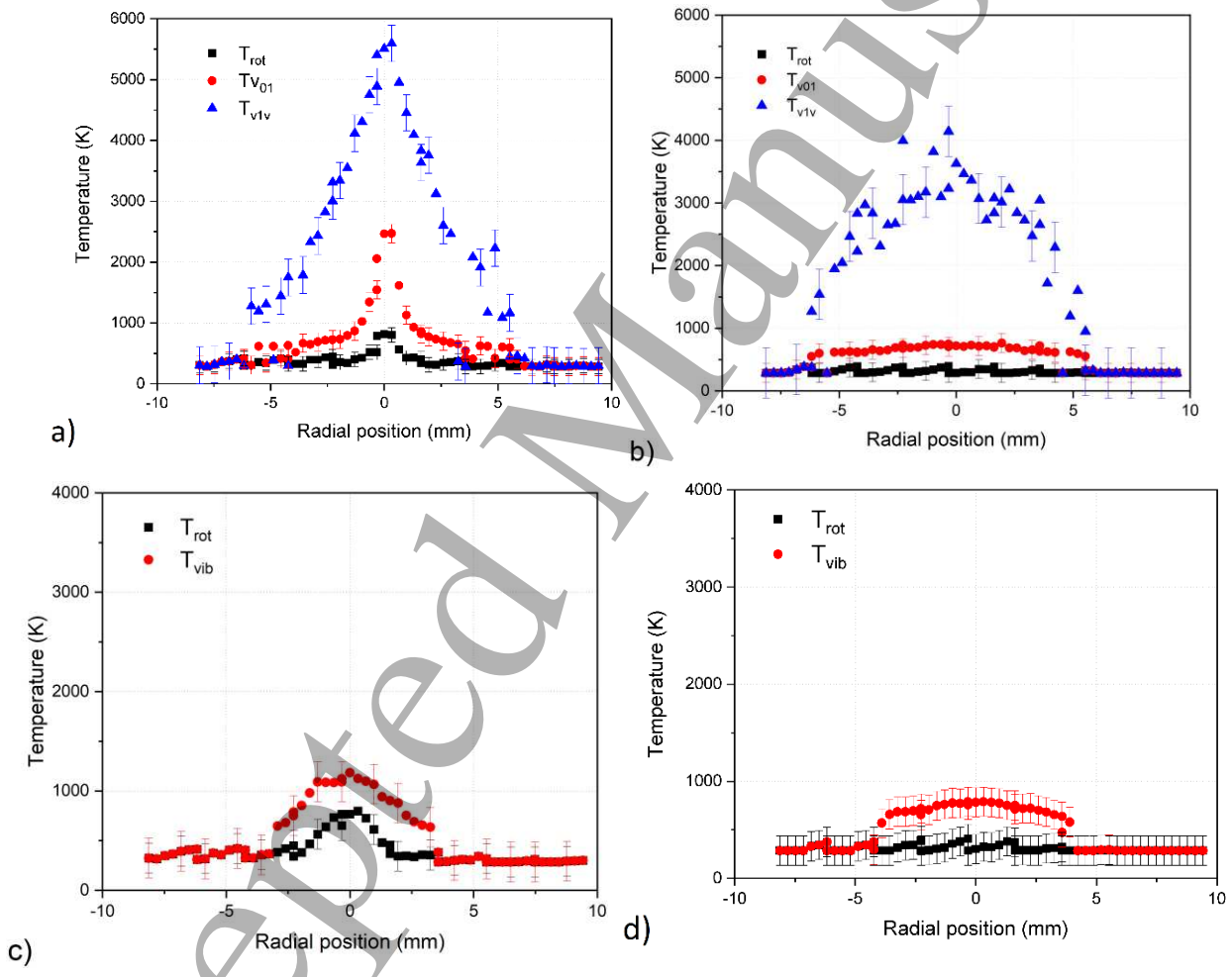

Figure 8: Radial profiles of rovibrational temperatures of $N_2(X,v)$ at 85 kV (channel 1) in ambient air at 1.5 mm from the pin in the first 300 ns a) and at 500 µs c) and at 9 mm from the pin in the first 300 ns b) and at 500 µs d).

5. Densities and pressure temporal profiles

The temporal evolution of the densities of molecular nitrogen and oxygen are presented in Figure 9.

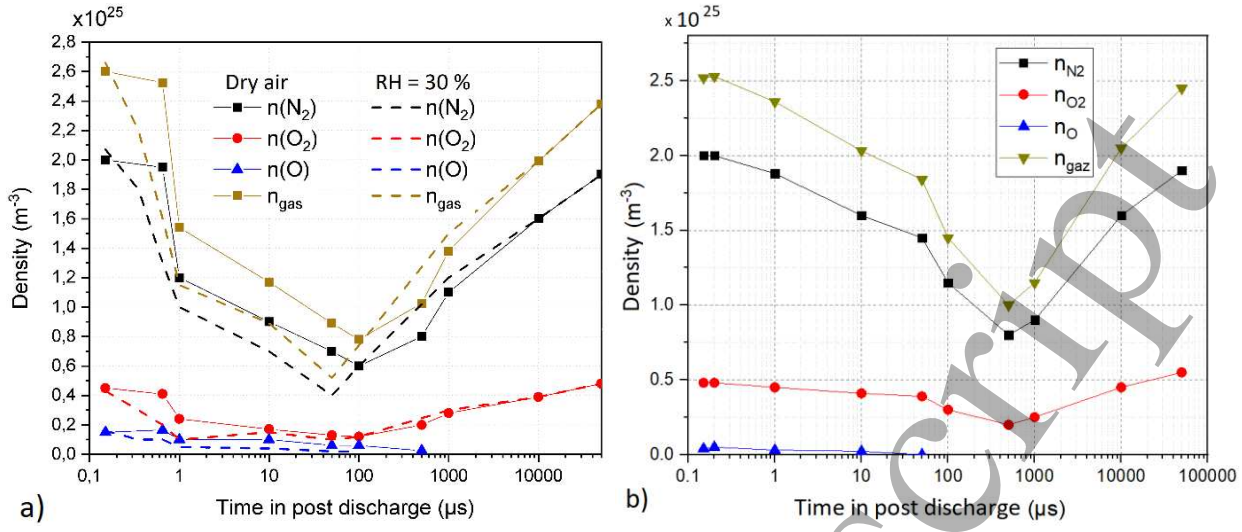

Figure 9: Temporal evolution of the densities of N_2, O_2 and O for a pulse of 85 kV (channel 1) at 1.5 mm in dry and ambient air a) and at 2.5 mm in dry air b).

During the first 500 ns of the post-discharge, molecular densities are not affected by fast heating which is therefore considered isochore. Then, the density is proportional to the inverse of the temperature. However, the values of the densities are affected by the dissociation of nitrogen and oxygen. The dissociation of nitrogen is weak since the density measured by Raman scattering at 150 ns, is equal to the density in air without discharge, considering the uncertainty of the measurement. Moreover, atomic nitrogen lines have been observed by emission spectroscopy only in the first millimetre close to the pin. The dissociation of oxygen is significant at 1.5 mm from the pin with 15 % dissociation in dry air in the first instants and 5 % at 2.5 mm (Figure 10 a). Despite the coherence and repeatability of the measurements, those rates are defined with a factor 2, coming from uncertainties on the density of nitrogen and oxygen (uncertainty on the determination of the temperature, on the spectroscopic constants and on the quality of the signals) and the hypothesis of the method (no dissociation of nitrogen). There is a strong gradient of the dissociation rate along the axis of the discharge since the dissociation is below the detection limit at the centre of the gap. The density of atomic oxygen at RH<2% and RH=30% in the first 500 ns of the post-discharge are relatively similar, within the uncertainty (Figure 10 a). The dissociation of atomic oxygen mainly comes from the quenching of excited states of nitrogen with molecular oxygen and from electron impact and dominant losses happen on much longer time scales (microseconds at least).

Between 500 ns and 10 µs, a shock wave develops radially which re-establishes atmospheric pressure at the centre (Figure 10 b)). It comes with gas expansion, the total density n_{gaz} decreasing from 2.5 to 1.5 10^{25} m^{-3} in 1 µs. Between 50 and 500 µs, the gas expansion is accentuated by the heating coming from V-T transfers. At 1.5 mm from the pin, in dry air, the density of nitrogen reaches a minimum of 6×10^{24} m^{-3} at 100 µs, when the temperature reaches 1200 K and 8×10^{24} m^{-3} at 2.5 mm where the temperature is about 400 K ± 200 K.

At 100 µs, a slight increase of pressure is observed. It cannot be due to the arrival of a shock wave coming from the plane because it arrives at latter times. It is more probably an artefact due to the large uncertainty in the temperature measurement at these post-discharge times. Indeed, the density of the gas being low at 100 and 500 µs because of the high temperatures, the Raman signal and therefore the signal-to-noise ratio is low and the adjustment of the spectra is more uncertain.

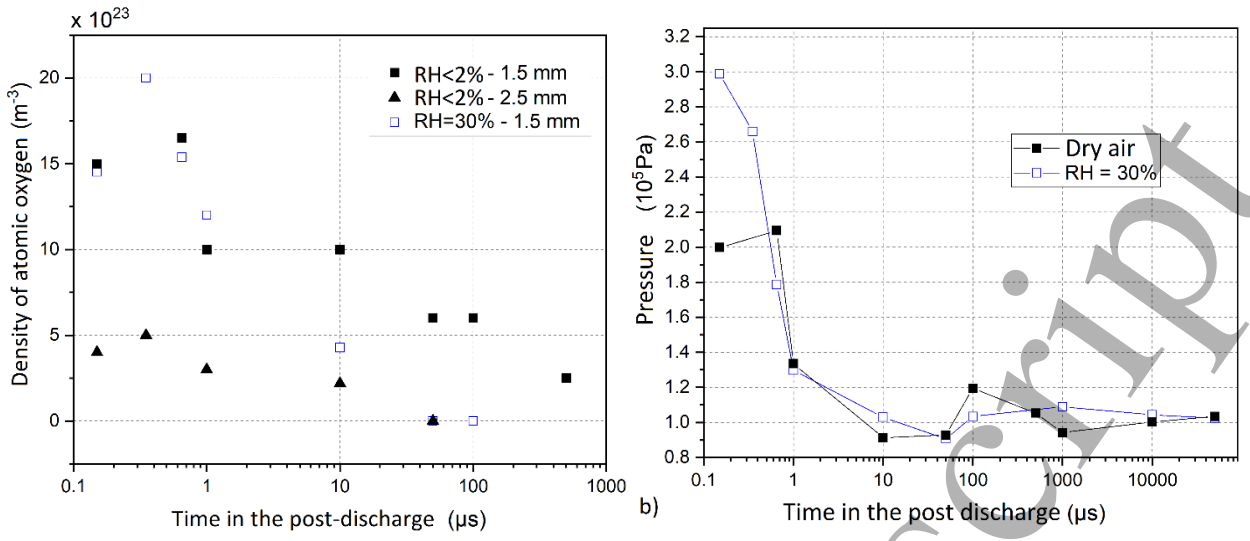

Figure 10: Temporal evolution of the density of atomic oxygen a) and of the gas pressure b) at 85kV (channel 1), at 1.5 mm from the pin, in dry and ambient air (RH<2% and RH=30 %).

Let us focus on the characteristic decay times of measured atomic oxygen density in Figure 10 a). In dry air, it is of the order of 500 µs at 1.5 mm from the pin and 100 µs at 2.5 mm. In humid air (RH=30%), it is 200 µs at 1.5 mm. In dry air, the atomic oxygen is converted into ozone or recombines with ozone and oxygen in a tenth of µs at room temperature and a few hundred microseconds at 1000 K. Dominant reactions involving atomic oxygen in the post discharge are detailed in Table 1.

Table 1: Dominant reactions involving atomic oxygen in the post-discharge.

$O(^3P) + O_2 + M \rightarrow O_3 + M$	$k_{M=O_2} = 0.69 \times 10^{-45} \times \left(\frac{300}{T_G}\right)^{1.28} [m^6/s]$ $k_{M=N_2} = 0.62 \times 10^{-45} \times \left(\frac{300}{T_G}\right)^{2} [m^6/s]$	[42,43]	(15)
$O + O + M \rightarrow O_2 + M$	$k_{M=O_2} = 0.241 \times 10^{-42} \times T_G^{-0.63} [m^6/s]$ $k_{M=N_2} = 0.27 \times 10^{-45} \times e^{720/T_G} [m^6/s]$	[43]	(16)
$O + O_3 \rightarrow O_2 + O_2$	$k = 0.12 \times 10^{-15} [m^3/s]$	[43]	(17)
$O + O_3 \rightarrow 2\,O + O_2$	$k = 0.12 \times 10^{-15} [m^3/s]$	[43]	(18)
$O_3 + N_2 \rightarrow O_2 + O + N_2$	$k = 0.73 \times 10^{-15} e^{-11400/T_g} [m^3/s]$	[42]	(19)
$O_3 + O_2 \rightarrow O_2 + O + O_2$	$k = 0.73 \times 10^{-15} e^{-11400/T_g} [m^3/s]$	[42]	(20)

An increase of temperature slows down the loss of atomic oxygen through ozone conversion. The temperature measured by Raman scattering at 1.5 mm from the pin and at 2.5 mm is approximately 1200 K and approximately 480 K, respectively at 100 µs. The recombination is faster at high temperature and the k rate is 5×10^{-46} m^6s^{-1} for N_2 and 2.8×10^{-45} m^6s^{-1} for O_2 at 1200 K. This corresponds to an oxygen recombination time of $1/(k_{N2}[O][N_2]+ k_{O2}[O][O_2]) \approx 200$ µs for a density of atomic oxygen of 0.5×10^{24} m^{-3} at 100 µs measured at 1.5 mm. The experimental decay time estimated is 500 µs. At 2.5 mm, the temperature is estimated to be about 480 K at 100 µs and it is the ozone-forming reaction that leads to the shortest decay rate, about 250 µs. These orders of magnitude are coherent with the $O(^3P)$ decay times measured in the diffuse discharge.

Between dry and humid air, there could also be an effect of temperature. At 1.5 mm from the pin, the gas temperature is initially 500 K in dry air and 800 K in the humid air and then reaches about 1200 K at about 50 to 100 µs in both cases. The increase of temperature due to humidity having the opposite effect of the one observed on the decay time, another phenomenon must therefore further increase the consumption of atomic oxygen density. In [9], it has been shown that in the presence of 2 % water vapour, the concentration of $O(^3P)$ is lower than in the presence of only 0.1% water vapour due to the OH and oxygen quenching with OH and H_2O by reactions (11) followed by (12), by reaction (9) and:

$$OH + O(^3P) \rightarrow O_2(v) + H \quad (21)$$

These reactions represent important losses of atomic oxygen during the post-discharge and could express temporal evolutions observed in Figure 10.

6. Energy partitioning between internal modes of nitrogen molecules

The post-discharge relaxation mechanisms are dependent on the gas and the shape of the voltage pulse. Let us determine, in the case of nitrogen, the amount of energy (eV/molecule) stored in the different internal storage modes of the molecule (vibration, translation) under these conditions. In particular, we can compare the energy distribution obtained with channels 1 and 2 at 85 kV in ambient air.

The average kinetic energy and the mean vibration energy of the nitrogen molecules are respectively determined as:

$$E_{cin} = E_{trans} + E_{rot} = 5/2\ kT \quad (22)$$

$$E_{vib} = \sum_v \sum_J f_{v,J}(T, T_{v01}, T_{v1v}) \times [E_{vib}(v) - E_{vib}(v=0)]hc \quad (23)$$

where $f_{v,J}(T, T_{v01}, T_{v1v})$ is the rovibrational distribution function of $N_2(X,v)$ which is measured by Raman scattering and $E_{vib}(v)$ is the vibrational energy of the vibrational level v, which is tabulated in the NIST database [44].

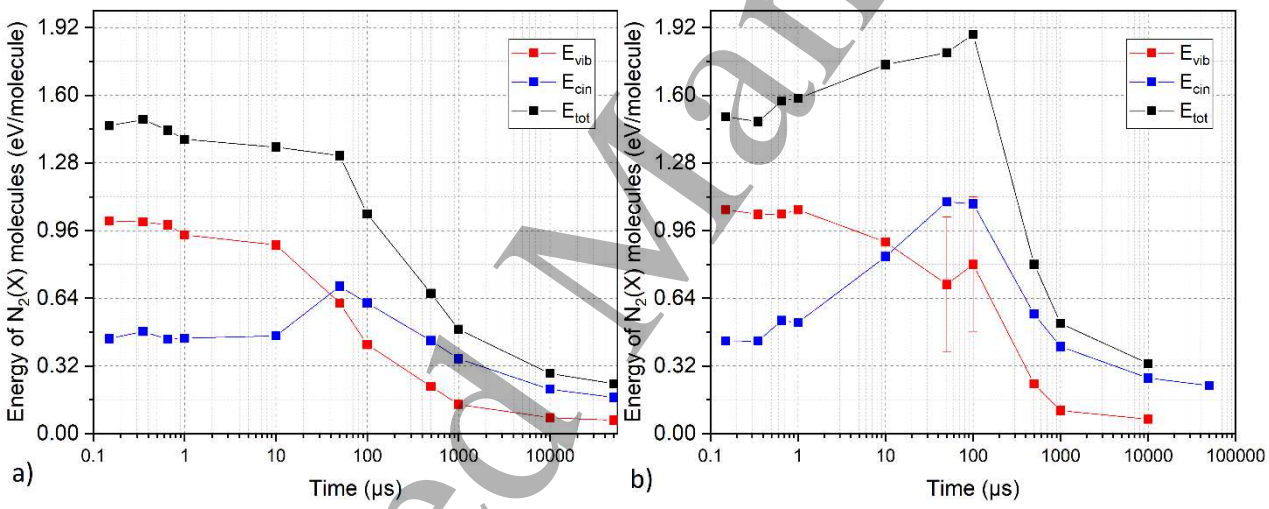

Figure 11: Temporal evolution of kinetic and mean vibrational energies of nitrogen molecules during the post-discharge for a pulse of 85 kV, for channels 1 a) and 2 b), at 1.5 mm from the pin, in ambient air.

In channel 1, the translational energy remains constant as long as the V-T processes are not significant (Figure 11 a). Up to 10 µs, the kinetic energy by molecule of nitrogen is 0.48 eV/molecule. At the beginning of the post-discharge, the part of the energy which is stored into vibrational levels is about three times higher. After 1 µs, the shock wave has induced a measurable decrease of the vibrational energy of nitrogen. Between 10 and 500 µs, the V-T transfers induce an important heating of the gas: the decrease in vibrational energy gets along with a significant rise of the kinetic energy which reaches 0.65 eV/molecule. After 50 µs, as much energy is stored in kinetic and in vibrational modes. After 500 µs, diffusion reduced the kinetic energy and the gas is completely relaxed after a few tens of milliseconds.

If in ambient air, just after the discharge, one third of the energy of $N_2(X)$ molecules is kinetic at 1.5mm from the pin, it represents only 10 % in dry air (not shown here). Therefore, in channel 1, in dry air, the proportion of energy used to heat the gas is considerably limited. This trend is confirmed by the numerical model in [9] already discussed, predicting similar estimations in dry and humid air.

Worth noting that the percentage of vibrational energy in relation to the total energy of a molecule describes only the energy stored in the vibrational levels of N_2 and the kinetic energy. It cannot account for the importance of other kinetic processes (dissociation, ionization…) compared to vibrational excitation. Thus, it is not a derivation of the percentage of electrical energy dissipated into $N_2(v)$ but more simply the energy partitioning between vibrational energy and kinetics of $N_2(X)$.

Compared to the discharge in [24] (dry air), since the diffuse discharge heats less, the energy is preferentially stored in the vibrational levels of $N_2(X)$. In [24], only 48 % of the energy is stored in $N_2(v)$, 2 % in $O_2(v)$ and 19 % in fast heating.

7. Conclusion

The rovibration excitation and relaxation mechanisms of nitrogen in the high-voltage diffuse discharge are very standard. During the discharge, nitrogen is excited by electronic impact and by quenching of excited states such as $N_2(A)$. The vibrational distribution is out of equilibrium and is characterized by two vibrational temperatures. One describes the first vibrational levels 0 and 1, the second describes all the other vibrational levels ($v > 1$) which are overpopulated compared to a Boltzmanian distribution. Vibrational equilibrium is established within 10 to 50 µs under the effect of V-V transfers. Then the energy stored in these vibrational modes is converted into kinetic energy by the V-T transfers in 100 to 500 µs. On the other hand, the initial rovibrational excitation is inhomogeneous along the axis. The gas temperature reaches up to about 1200 K close to the pin (85 kV, ambient air) while it remains below 500 K in the rest of the volume.

It has been shown that both the voltage amplitude and the duration of the voltage pulse control the vibrational excitation and heating of the discharge. Thus, by increasing the FWHM of the voltage pulse from 5 to 10 ns, the gas temperature increases from 1200 to 2000 K after V-T relaxation. Therefore, it is possible to control the heating of the discharge without profoundly modifying the energy transfer mechanisms by adjusting the duration of the voltage pulse. The spatial distribution of the rovibrational excitation of the diffuse discharge is very wide radially, consistent with the sustainability of fields greater than 100 Td over nearly 8 mm during propagation. As the gas expands under heating, the rovibrational excitation of the molecules expands slightly during the post-discharge.

The main effects of humidity is to amplify the fast heating and to accelerate the decay of atomic oxygen in the post-discharge. The former effect is mainly due to the exothermic formation of the OH molecules and the very fast V-T transfer of the water molecules (a few tens of ns). No significant acceleration of the V-T relaxation of nitrogen due to the addition of water vapour was observed for the studied conditions.

Density and temperature measurements allowed to determine the pressure in the gas (about 2 bar in dry air at the pin and 3 bar in ambient air) and to identify the start of a shock wave around 500 ns. The atomic oxygen density is also estimated at 1.5 mm from the pin (where the density is sufficient) to 1.6×10^{24} m^{-3} corresponding to about 20 % dissociation.

It thus appears that the main differences with the lower field discharges are rather visible at the beginning of the discharge with a specific spatial volume distribution and a significant vibrational non-equilibrium between v=0,1 and v>1. The vibrational excitation of nitrogen molecules remains high despite the strong electric fields applied during the discharge itself and the relaxation processes are similar. In terms of reactivity, high atomic oxygen densities seem to be very localized in the vicinity of the pin (10^{24} m^{-3}). This inhomogeneity reflects the distribution of energy in the volume of the discharge. In order to determine whether the high-voltage diffuse discharge induces more reactive kinetics than moderate-voltage filamentary discharges, the energy expended in the vibrational excitation of $N_2(X)$ should still be accurately determined in relation to the total energy dissipated in the discharge. Also, much more precise measurements of the density of nitrogen and atomic oxygen by TALIF for example are needed to better describe the reactive regions of the plasma.

In the context of applications, the low temperatures measured for shortest voltage pulses can be interesting for some pollution control or flow control applications. In the field of assisted combustion, on the contrary, discharges of longer duration would be more favourable. In this respect, it would be interesting to deepen the study on the influence of the voltage pulse width and to determine the influence of the rate of the voltage rise on rovibration excitation and heating.

Acknowledgements

This work is supported by the Agence Nationale de la Recherche in the frame of the ANR-13-BS09-0014 research program.

References

[1] Rep'ev A G and Repin P B 2006 Dynamics of the optical emission from a high-voltage diffuse discharge in a rod-plane electrode system in atmospheric-pressure air *Plasma Phys. Rep.* **32** 72–8

[2] Tardiveau P, Magne L, Marode E, Ouaras K, Jeanney P and Bournonville B 2016 Sub-nanosecond time resolved light emission study for diffuse discharges in air under steep high voltage pulses *Plasma Sources Sci. Technol.* **25** 054005

[3] Naidis G V, Tarasenko V F, Babaeva N Y and Lomaev M I 2018 Subnanosecond breakdown in high-pressure gases *Plasma Sources Sci. Technol.* **27** 013001

[4] Stepanyan S A, Soloviev V R and Starikovskaia S M 2014 An electric field in nanosecond surface dielectric barrier discharge at different polarities of the high voltage pulse: spectroscopy measurements and numerical modeling *J. Phys. D: Appl. Phys.* **47** 485201

[5] Brisset A, Gazeli K, Magne L, Pasquiers S, Jeanney P, Marode E and Tardiveau P 2019 Modification of the electric field distribution in a diffuse streamer-induced discharge under extreme overvoltage *Plasma Sources Science and Technology* **28** 055016

[6] Chng T L, Brisset A, Jeanney P, Starikovskaia S M, Adamovich I V and Tardiveau P 2019 Electric field evolution in a diffuse ionization wave nanosecond pulse discharge in atmospheric pressure air *Plasma Sources Science and Technology* **28** 09LT02

[7] Stancu G, Kaddouri F, Lacoste D and Laux C Investigations of the Rapid Plasma Chemistry Generated by Nanosecond Discharges in Air at Atmospheric Pressure Using Advanced Optical Diagnostics *40th AIAA Plasmadynamics and Lasers Conference* (American Institute of Aeronautics and Astronautics)

[8] Marode E, Djermoune D, Dessante P, Deniset C, Ségur P, Bastien F, Bourdon A and Laux C 2009 Physics and applications of atmospheric non-thermal air plasma with reference to environment *Plasma Phys. Control. Fusion* **51** 124002

[9] Komuro A and Ono R 2014 Two-dimensional simulation of fast gas heating in an atmospheric pressure streamer discharge and humidity effects *J. Phys. D: Appl. Phys.* **47** 155202

[10] Ono R, Takezawa K and Oda T 2009 Two-photon absorption laser-induced fluorescence of atomic oxygen in the afterglow of pulsed positive corona discharge *Journal of Applied Physics* **106** 043302

[11] Popov N A 2011 Fast gas heating in a nitrogen–oxygen discharge plasma: I. Kinetic mechanism *J. Phys. D: Appl. Phys.* **44** 285201

[12] Stancu G D, Kaddouri F, Lacoste D A and Laux C O 2010 Atmospheric pressure plasma diagnostics by OES, CRDS and TALIF *J. Phys. D: Appl. Phys.* **43** 124002

[13] Pasquiers S, Bentaleb S, Jeanney P, Blin-Simiand N, Tardiveau P, Magne L, Godanna K, Moreau N and Jorand F 2013 Towards a kinetic understanding of the ignition of air-propane mixture by a non-equilibrium discharge: the decomposition mechanisms of propane *IJAD* **3**

[14] Ouaras K, Magne L, Pasquiers S, Tardiveau P, Jeanney P and Bournonville B 2018 OH density measured by PLIF in a nanosecond atmospheric pressure diffuse discharge in humid air under steep high voltage pulses *Plasma Sources Sci. Technol.* **27** 045002

[15] Bruggeman P and Schram D C 2010 On OH production in water containing atmospheric pressure plasmas *Plasma Sources Sci. Technol.* **19** 045025

[16] Winters C, Hung Y-C, Jans E, Eckert Z, Frederickson K, Adamovich I V and Popov N 2017 OH radical kinetics in hydrogen-air mixtures at the conditions of strong vibrational nonequilibrium *J. Phys. D: Appl. Phys.* **50** 505203

[17] Frederickson K, Hung Y-C, Lempert W R and Adamovich I V 2016 Control of vibrational distribution functions in nonequilibrium molecular plasmas and high-speed flows *Plasma Sources Sci. Technol.* **26** 014002

[18] Starikovskiy A and Aleksandrov N 2013 Plasma-assisted ignition and combustion *Progress in Energy and Combustion Science* **39** 61–110

[19] Xu D A, Lacoste D A and Laux C O 2016 Ignition of Quiescent Lean Propane–Air Mixtures at High Pressure by Nanosecond Repetitively Pulsed Discharges *Plasma Chem Plasma Process* **36** 309–27

[20] Lo A, Frat F, Domingues E, Lacour A, Lecordier B, Vervisch P and Cessou A 2017 Nanosecond pulsed discharge in a propane–air mixture: Ignition and energy deposition *Proceedings of the Combustion Institute* **36** 4087–94

[21] Galley D, Pilla G, Lacoste D, Ducruix S, Laux C, Lacas F and Veynante D 2005 Plasma-Enhanced Combustion of a Lean Premixed Air-Propane Turbulent Flame using a Nanosecond Repetitively Pulsed Plasma *43rd AIAA Aerospace Sciences Meeting and Exhibit* Aerospace Sciences Meetings (American Institute of Aeronautics and Astronautics)

[22] Choi W-S, Neumeier Y and Jagoda J 2004 Stabilization of a Combustion Process near Lean Blow Off by an Electric Discharge *42nd AIAA Aerospace Sciences Meeting and Exhibit* Aerospace Sciences Meetings (American Institute of Aeronautics and Astronautics)

[23] Tardiveau P, Bentaleb S, Jeanney P, Jorand F and Pasquiers S 2012 Comparative Study of Air-Propane and Air-Heptane Mixtures Ignition by Nanosecond Pulsed Discharges *International Journal of Plasma Environmental Science & Technology* **6** 130–4

[24] Lo A, Cessou A, Boubert P and Vervisch P 2014 Space and time analysis of the nanosecond scale discharges in atmospheric pressure air: I. Gas temperature and vibrational distribution function of N2and O2 *J. Phys. D: Appl. Phys.* **47** 115201

[25] Lo A, Cessou A and Vervisch P 2014 Space and time analysis of the nanosecond scale discharges in atmospheric pressure air: II. Energy transfers during the post-discharge *J. Phys. D: Appl. Phys.* **47** 115202

[26] Vereshchagin K A, Smirnov V V and Shakhatov V A 1997 CARS study of the vibrational kinetics of nitrogen molecules in the burning and afterglow stages of a pulsed discharge *Tech. Phys.* **42** 487–94

[27] Filimonov S and Borysow J 2007 Vibrational and rotational excitation within theX\hspace0.167em1${upSigma *J. Phys. D: Appl. Phys.* **40** 2810–7

[28] Popov N, Babaeva N and Naidis G 2019 Recent advances in the chemical kinetics of non-equilibrium plasmas *J. Phys. D: Appl. Phys.* **52** 160301

[29] Komuro A, Ono R and Oda T 2010 Kinetic model of vibrational relaxation in a humid-air pulsed corona discharge *Plasma Sources Sci. Technol.* **19** 055004

[30] Teramoto Y and Ono R 2014 Measurement of vibrationally excited N2(v) in an atmospheric-pressure air pulsed corona discharge using coherent anti-Stokes Raman scattering *Journal of Applied Physics* **116** 073302

[31] Ono R, Teramoto Y and Oda T 2009 Effect of humidity on gas temperature in the afterglow of pulsed positive corona discharge *Plasma Sources Sci. Technol.* **19** 015009

[32] Tardiveau P, Magne L, Marode E, Ouaras K, Jeanney P and Bournonville B 2016 Sub-nanosecond time resolved light emission study for diffuse discharges in air under steep high voltage pulses *Plasma Sources Sci. Technol.* **25** 054005

[33] Ajrouche H, Lo A, Vervisch P and Cessou A 2015 Assessment of a fast electro-optical shutter for 1D spontaneous Raman scattering in flames *Meas. Sci. Technol.* **26** 075501

[34] Lo A, Cléon G, Vervisch P and Cessou A 2012 Spontaneous Raman scattering: a useful tool for investigating the afterglow of nanosecond scale discharges in air *Appl. Phys. B* **107** 229–42

[35] Montello A, Yin Z, Burnette D, Adamovich I V and Lempert W R 2013 Picosecond CARS measurements of nitrogen vibrational loading and rotational/translational temperature in non-equilibrium discharges *J. Phys. D: Appl. Phys.* **46** 464002

[36] Aleksandrov N L, Kindysheva S V, Nudnova M M and Starikovskiy A Y 2010 Mechanism of ultra-fast heating in a non-equilibrium weakly ionized air discharge plasma in high electric fields *J. Phys. D: Appl. Phys.* **43** 255201

[37] Marode E 1975 The mechanism of spark breakdown in air at atmospheric pressure between a positive point and plane. II. Theoretical: Computer simulation of the streamer track *Journal of Applied Physics* **46** 2016–20

[38] Ono R, Teramoto Y and Oda T 2009 Effect of humidity on gas temperature in the afterglow of pulsed positive corona discharge *Plasma Sources Sci. Technol.* **19** 015009

[39] Brisset A, Tardiveau P, Gazeli K, Bournonville B, Jeanney P, Ouaras K, Magne L and Pasquiers S Influence of water vapor content in air on the dynamics of a high electric field non-equilibrium diffuse discharge *J. Phys. D: Appl. Phys. (under submission)*

[40] Tsuchiya M, Tashiro T and Shigihara A 2004 Water Clusters in Gas Phases Studied by Liquid Ionization Mass Spectrometry *Journal of the Mass Spectrometry Society of Japan* **52** 1–12

[41] Komuro A, Takahashi K and Ando A 2015 Vibration-to-translation energy transfer in atmospheric-pressure streamer discharge in dry and humid air *Plasma Sources Sci. Technol.* **24** 055020

[42] Pignolet P, Hadj-Ziane S, Held B, Peyrous R, Benas J M and Coste C 1990 Ozone generation by point to plane corona discharge *J. Phys. D: Appl. Phys.* **23** 1069–72

[43] Kossyi I A, Kostinsky A Y, Matveyev A A and Silakov V P 1992 Kinetic scheme of the non-equilibrium discharge in nitrogen-oxygen mixtures *Plasma Sources Sci. Technol.* **1** 207–20

[44] National Institute of Standards and Technology *NIST*